RESEARCH ARTICLE

# Enhanced Electrochemical Reduction of $CO_2$ by Zeolitic Imidazolate Frameworks-8 Supported Silver Nanoparticles

**Zhihong Zhuang, Yicheng Zhang, Liang Hu, Jianli Wang, Zhao Zhang, Weiqiang Han***

School of Materials Science and Engineering, Zhejiang University, 38 Zheda Road, Hangzhou, 310027, Zhejiang, People's Republic of China

***Corresponding author: E-mail: hanwq@zju.edu.cn**

**DOI: 10.5185/amlett.2020.081546**

**Silver (Ag) is a typical catalyst for $CO_2$ electroreduction. To improve the CO faradaic efficiency, ZIF-8 supported thiol-capped Ag nanoparticles (Ag NPs) of about 3.9 nm were facilely synthesized by reducing $Ag^+$ in ZIF-8 suspension in the presence of thiol-containing mercaptopropionic acid (MPA) molecules. MPA can induce the monodisperse Ag NPs formation, cap on the surface of Ag NPs and immobilize on ZIF-8 through coordinating with the unsaturated $Zn^{2+}$ cations. The Ag/ZIF-8 can efficiently reduce $CO_2$ to CO with a maximum CO faradaic efficiency of 92.3% at the potential of –0.88 V (vs. RHE), higher than that of ZIF-8 and Ag/C. The performance improvement in $CO_2$ electroreduction over Ag/ZIF-8 is probably attributed to the small-size of Ag NPs and the synergistic effect between Ag NPs and ZIF-8.**

## Introduction

The growing consumption of fossil resource since the first industrial revolution contributes to a large amount of carbon dioxide ($CO_2$) emissions to the atmosphere [**1**], which leads to several environmental problems, especially the global warming [**2**]. As $CO_2$ is the main origin of global warming, conversion of $CO_2$ into a clean energy source is considered to be a promising way to solve the emergent energy and environmental issues. Among various methods of utilizing and converting $CO_2$, the electrochemical reduction of $CO_2$ ($CO_2$RR) seems to be a promising strategy to simultaneously realize carbon cycle utilization and renewable energy storage for its clean, sustainable and effective properties [**3**].

CO, HCOOH and other hydrocarbon products have been reported as reduction products determined by the nature of the metal electrode that was used [**3**]. CO is one of the most common and desirable products from $CO_2$ reduction since it is a key starting material to synthesize other useful chemicals and fuel through, for example, the Fischer-Tropsch process [**1**]. However, $CO_2$ is a thermodynamically stable molecule, which needs a suitable catalyst to activate with significantly reduced energy penalty. In the field of metal-catalysts (e.g., Au, Ag, Pd and Zn), [**4-8**] Ag has attracted much attention because it gives a compromise between the cost and $CO_2$RR performance. To further improve the catalytic performance of Ag, researchers devote much effort to tuning the size and shape of Ag catalyst [**9-10**], forming silver alloy [**11**] or various nanostructures [**12-13**]. Ag nanoparticles (Ag NPs) show good selectivity and catalytic activity in the past studies [**10**], but it is not easy to prepare ultrafine Ag NPs, because they possess high surface energy and readily aggregate during the reduction reaction. It is necessary to simplify the nanofabrication of Ag particles and enhance the $CO_2$RR performance of Ag NPs.

Metal-organic frameworks (MOFs), combining the favorable characteristics of heterogeneous and homogeneous catalysts, have been explored as a novel class of model catalytic materials for understanding $CO_2$RR. Zeolitic imidazolate framework-8 (ZIF-8) was first used as a catalytic material for $CO_2$RR as reported by Yulin Wang *et al.*, and delivered moderate catalytic activity with 65% CO yield [**14**]. Nikolay Kornienko et al. introduced a cobalt−porphyrin MOF, i.e., $Al_2(OH)_2$TCPP -Co, as an electrocatalyst for $CO_2$RR, which reveals a selectivity toward CO production more than 76% and stability over 7 h [**15**]. Xinhe Bao's group found that ZIF-8 outperforms other structurally similar MOF catalysts (ZIF-8, ZIF-108, ZIF-7 and SIM-1) in $CO_2$RR, exhibiting a maximum CO Faradaic efficiency of 81% at −1.1V (vs. RHE) [**16**]. However, there is still a large space for further improvement in the MOF-catalyzed $CO_2$RR [**15**].

In this study, ultrafine Ag NPs uniformly decorated ZIF-8 (Ag/ZIF-8) was obtained by reducing $Ag^+$ in ZIF-8 suspension in the presence of thiol-containing mercaptopropionic acid (MPA) molecules for electrochemical reduction of $CO_2$ to CO. The Ag NPs were capped with thiol groups from MPA and immobilize on ZIF-8 with the help of MPA. With the cooperation of ZIF-8 and Ag NPs, Ag/ZIF-8 exhibited apparently increased current density with the CO Faradaic efficiency increasing to 92.3%. Besides, the Ag/ZIF-8 catalyst showed higher CO Faradaic efficiency than Ag/C and ZIF-8. Overall, the strategy developed here demonstrated a novel and

convenient route to synthesize supported small-sized Ag NPs to enhance $CO_2$RR performance of Ag.

## Experimental section

### Materials

Nafion solution (5 wt%) was purchased from Shanghai Hesen Electric Company. 2-methylimidazole (2-MeIM, 99%) was obtained from Aladdin Corporation. Potassium chloride (KCl >99.5%), zinc nitrate hexahydrate ($Zn(NO_3)_2{\cdot}6H_2O$, 98%), ethylene glycol (EG, 99.8%), absolute ethanol, silver nitrate ($AgNO_3$, 99.8%) and methanol (>99.8%) were purchased from Sinopharm Chemical Reagant Corporation. 3-mercaptopropionic acid (MPA, 99%) was obtained from Damas Beta Corporation. Sodium borohydride ($NaBH_4$, 99%) was purchased from Alfa Aesar Corporation. Vulcan XC-72R carbon black was obtained from Cabot Corporation. All electrolytes were prepared using deionized water. The above chemicals were used as received without further purification.

### Catalyst synthesis

#### *Synthesis of ZIF-8*

The synthesis of ZIF-8 was modified from a previous report [**17**]. Typically, zinc nitrate hexahydrate (2.975 g) and 2-methylimidazole (3.284 g) were separately dissolved in methanol (100 mL) and then mixed together under vigorous stirring for 5 min. The solution was stirred at room temperature for 12 h. After that, white powders were collected by centrifugation, washed several times with methanol, and dried overnight at 60°C.

#### *Synthesis of Ag/ZIF-8 and Ag/C*

30 mL $AgNO_3$ methanol solution and MPA methanol solution were mixed at a $AgNO_3$/MPA molar ratio of 1:3. The solution was stirred for 3 hours at room temperature, and white turbidity was collected by centrifugation and purified using ethanol to remove unreacted reagent. The product was finally dispersed in 8.0 mL of methanol by sonication and stirring, forming MPA-Ag solution.

The Ag/ZIF-8 was prepared by the following steps: 0.25 g ZIF-8 nanoparticles and 3 mL MPA-Ag solution were added to 60 mL methanol. The suspension was sonicated for 15 min and then stirred for 2.5 h at room temperature. After that, 15 mL of 0.5M $NaBH_4$ methanolic solution was prepared and injected into the above solution under vigorous stirring. After stirring for 1.5 h, the precipitate was collected by centrifuging, purified using ethanol and deionized water to remove unreacted reagents and dried in a vacuum oven at 60°C over night. The obtained catalyst is denoted as Ag/ZIF-8. For comparison, the Ag NPs was also synthesized using the same procedures except that 0.25 g Vulcan XC-72R carbon black replaced ZIF-8 as the support, the obtain sample is denoted as Ag-C.

In order to obtain the similar size of Ag NPs. The Ag/C was synthesized using a modified protocol according to reference [**10**]. 26 mg of AgNO3 was dissolved in 15 mL of ethylene glycol (EG; Aldrich, 99.8%) with vigorous stirring and this solution was slowly heated to 50°C for 20 min. 250mg of carbon black (Vulcan XC-72R) was dispersed in 50 mL EG and 52 mg of MPA solution by ultrasonication for 30 min. The prepared carbon black solution was added to the silver precursor solution at 50°C, and the mixed solution was kept at 50°C for 10 min prior to heating to 160°C with a ramping rate of 3-4°C /min. The Ag/C were synthesized by controlling the maintaining time at 160°C for proper time. The precipitate was collected by centrifuging, purified using ethanol and deionized water to remove unreacted reagents and dried in a vacuum oven at 60°C over night. The obtained catalyst is denoted as Ag/C.

### Production analysis

The gas generating components were collected from the closed space above the cathode and analyzed by gas chromatography (GC 9790, FULI). The liquid product was collected and analyzed by $^1$H NMR spectroscopy. In our experiments, CO and $H_2$ were detected as the only products. Faradaic efficiency (FE) is calculated by the following formula:

$$FE = x\ n\ F/Q{*}100\ \%$$

where: x = number of electrons exchanged (for CO and $H_2$, x = 2)

n = the number of moles for specific product

F = Faraday's constant (96485 C/mol)

Q = the charge passed (C)

The partial current density for a specific product was calculated by multiplying total current density by Faradaic efficiency for this product.

### Characterization techniques

The crystalline structures were detected by power X-ray diffraction (XRD, Rigaku MiniFlex), with CuKα radiation (λ=1.5418Å) at 40 kV and 100 mA. Transmission electron microscopy (TEM) images was obtained on a FEI Tecnai G2 F20 S-TWIN instrument operated at 200 kV. Scanning transmission electron microscopy (STEM) image, energy-dispersive X-ray (EDX) spectra and STEM-EDX mapping were acquired with a FEI Tecnai G2 F20 S-TWIN instrument operated at 200kV. Scanning electron microscopy (SEM) image was obtained with a Hitachi SU-8010 SEM instrument. XPS (Thermo Scientific K-Alpha+) was utilized to detected the surface elemental chemical chemistry of catalysts with the adventitious carbon (C 1s) at the binding energy (BE) of 284.8 eV as the reference. The actual Ag loadings of different catalysts were measured by a Perking Elmer inductively coupled plasma optical emission spectrometer (ICP-OES, Agilent 720ES).

### Electrochemical performance

#### *Preparation of working electrode*

Catalyst-modified glassy carbon was used as work electrode. Firstly, 7 mg catalyst and 3 mg carbon black were dispersed in a mixture containing 200 μL ethanol, 80 μL deionized water and 20 μL 5% Nafion solution by sonicating for 30 min to form a homogeneous ink. Then, 20

μL of the catalyst ink was coated on a 1 × 1 $cm^2$ glassy carbon electrode and dried in ambient condition overnight. Finally, we obtain the catalyst-modified glassy carbon.

### *$CO_2$ Electrochemical reduction performance*

The electrochemical tests were performed with a CHI660E electrochemical workstation. All the electrochemical experiments were performed in H-type cell with two compartments (Figure S1) and three-electrode electrochemical setup. The cathodic and anodic compartment were separated by a Nafion N117 membrane. The catalyst-modified glassy carbon was used as working electrode. An Ag/AgCl electrode and a Pt net were used as the reference electrode and the counter electrode, respectively. Electrode potentials were iR corrected and converted to the reversible hydrogen electrode (RHE) scale using E (vs. RHE) = E (vs. Ag/AgCl) + 0.197V +0.0592 × pH. The electrolyte used for $CO_2$ reduction experiment was 0.5M KCl saturated with $CO_2$. The linear sweep voltammetry (LSV) of catalyst-modified GC electrode was performed in an Ar- or $CO_2$- saturated 0.5 M KCl aqueous electrolyte at room temperature with the scan rate of 10 mV/s.

## Result and discussion

The typical preparation route of Ag/ZIF-8 nanocomposites is shown in **Fig. 1a**, starting from the pristine ZIF-8. ZIF-8 was synthesized according to previous report with a little modified parameters [**17**]. In order to decorate the ZIF-8 with the Ag nanoparticles (Ag NPs) uniformly, we introduced 3-mercaptopropionic acid (MPA) as the capping agent during the $NaBH_4$-assisted reduction of $AgNO_3$, which contains a thiol group (−SH) and a carboxyl group ($-COO^-$) that are located at two ends of the MPA molecule. (**Fig. 1b**). In principle, the thiol group has stronger interactions with silver [**18**], meanwhile the carboxylate anions of MPA can coordinate with the unsaturated $Zn^{2+}$ cations on the exterior surface of ZIF-8 (**Fig. 1c**).

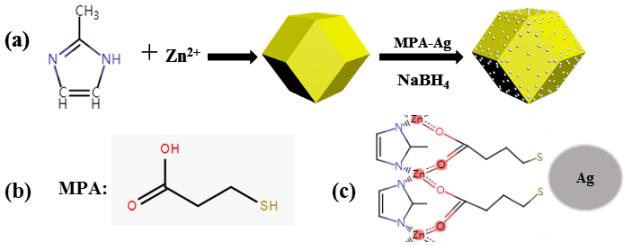


**Fig. 1.** (a) The typical preparation route of Ag/ZIF-8, (b) the molecular structure of MPA and (c) the interactions of Ag with ZIF-8.

**Fig. 2** shows that both ZIF-8 and Ag/ZIF-8 exhibit similar X-ray diffraction (XRD) peaks to the simulated ZIF-8 [**14**]. Compared with ZIF-8, Ag/ZIF-8 shows no significant loss of crystallinity and no supplementary Bragg peaks, indicating that the structure of ZIF-8 is maintained after decoration with Ag NPs. It is difficult to observe the peaks of Ag in the XRD pattern of Ag/ZIF-8 (**Fig. 2**), because these peaks are too weak due to the ultrafine sizes of Ag NPs and also overlap with the relatively strong peaks of ZIF-8. However, the Ag XRD peaks for carbon-supported Ag NPs (Ag-C) synthesized with a similar procedure, especially the peak at 38.1° that corresponds to the Ag (111) reflection are much easier to distinguish (Figure S2), due to the less intense XRD peaks of carbon black and/or larger size of Ag NPs. Furthermore, due to the high MPA/$Ag^+$ ratio during the preparation of Ag/ZIF-8 and Ag-C, some $Ag_2S$-like phase may exist [**19**], but can't be detected in the XRD pattern of Ag-C, let alone in that of Ag/ZIF-8.

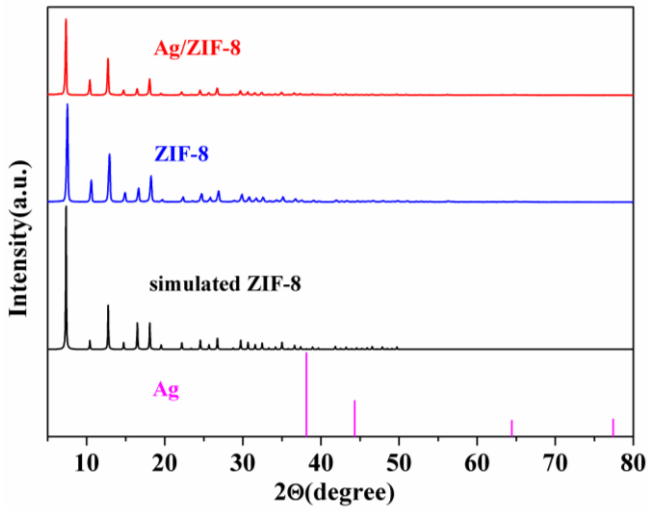


**Fig. 2.** XRD patterns of ZIF-8 and Ag/ZIF-8.

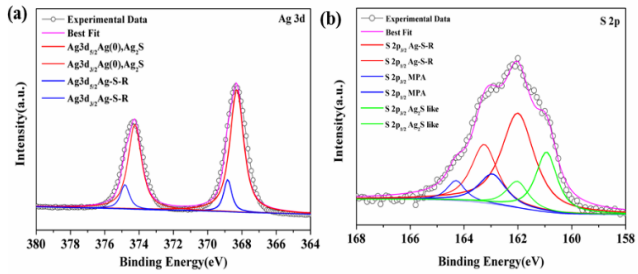


**Fig. 3.** High resolution XPS spectra of Ag/ZIF-8: (a) Ag 3d spectra and (b) S 2p spectra.

To investigate the structure of the MPA-bridged Ag/ZIF-8, X-ray photoelectron spectroscopy (XPS) was conducted. The comparison between the XPS survey spectra of ZIF-8 and Ag/ZIF-8 (Figure S3) confirms the presence of MPA and silver species in Ag/ZIF-8 due to its additional S 2p, Ag 3d and Ag 3p peaks. The high-resolution XPS spectra give more information (**Fig. 3**). The Ag $3d_{5/2}$ and Ag $3d_{3/2}$ double peaks in the Ag3d XPS spectrum are separated by a spin–orbit splitting of 6 eV (**Fig. 3a**). Ag/ZIF-8 possesses two main Ag 3d peaks at 374.3 and 368.3 eV (**Fig. 3a**), which reveals that metallic silver (Ag(0)) is the dominant silver species [**20**]. The second spin-orbit pair of small intensity at higher BE values (Ag $3d_{5/2}$ at about 369 eV, **Fig. 3a**) is attributed to the more oxidized surface Ag atoms bonding to MPA molecule through a Ag-S bond [**19**]. The possibly presented Ag ion

(Ag+) in $Ag_2S$ can't be distinguished because a Ag(0)−$Ag_2S$ peak separation is too small to be appreciated. There are three distinct chemical states for S shown in the S 2p spectra (**Fig. 3b**), where the $S2p_{3/2}$ and $S2p_{1/2}$ peaks were separated by a spin-orbit splitting of 1.2 eV. The S $2p_{3/2}$ peak at the BE of nearly 162 eV (the red line, **Fig. 3b**) is associated with an Ag-S bond which results from the interaction of organometallic thiols with Ag surface [**21**]. The S $2p_{3/2}$ signal close to 163 eV (the blue line, **Fig. 3b**) is due to sulfur atoms of physically adsorbed MPA molecules [**19**]. A spin-orbit bimodal with a lower BE value (BE $S2p_{3/2}$ component close to 161 eV, the green line in Figure 3b) can be associated with S in a chemical state like $Ag_2S$ [**19**]. The XPS technique confirms the existence of Ag2S-like phase in Ag/ZIF-8, overcoming the above-mentioned inability of XRD technique to detect this species. Therefore, the NPs on ZIF-8 is probably composed of metallic Ag and small amount of $Ag_2S$-like phase [**19**]. Despite this, we still label the NPs as Ag NPs.

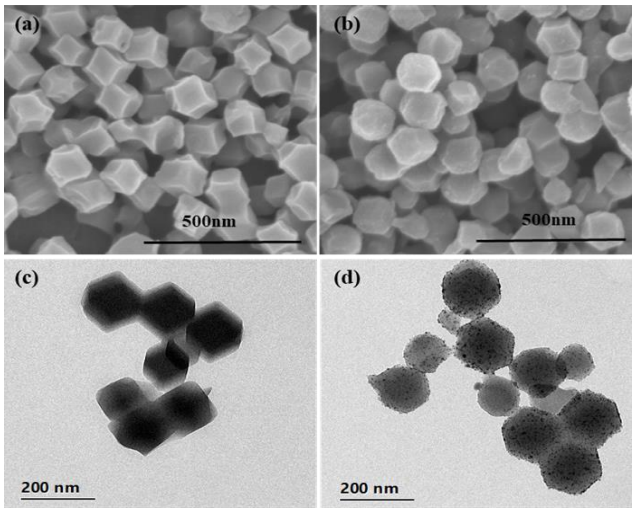


**Fig. 4.** SEM images of (a)ZIF-8 and (b)Ag/ZIF-8, and TEM images of (c) ZIF-8 and (d) Ag/ZIF-8.

**Fig. 4** displays the scanning electron microscopy (SEM) and transmission electron microscopy (TEM) images before and after the decoration of Ag NPs. **Fig. 4a** and **Fig. 4d** show the presence of ZIF-8 rhombohedral dodecahedrons with the size of about 100 nm. After being decorated with Ag nanoparticles, the main structure of ZIF-8 is well maintained (**Fig. 4b**). The TEM image clearly shows that Ag nanoparticles are uniformly distributed on the Ag/ZIF-8 (**Fig. 4d**) with an average size of 3.9 nm (Figure S4c). The crystal lattice spacing of the Ag/ZIF-8 is 0.23 nm (Figure S4b), which is consistent with the interplanar spacing of Ag (111) planes [**10**]. The electron diffraction also confirms the existence of Ag (Figure S4d). It can be seen from the FigureS4d that the electron diffraction pattern is ring-shaped and is accompanied by intermittent bright spots. The diffraction ring corresponds to the characteristic crystal planes of silver nanoparticles (111), (200), (220), (311). STEM-EDS mapping images (Figure S5) of the select area indicate the homogeneous dispersion of Ag and S atom on ZIF-8, but can't exclude the core-shell structure of Ag NPs. It worth noting that the Ag NPs in the abovementioned Ag-C (without ZIF-8) are also uniform and nanoscale (Figure S6a), but the average particle size is 8.15 nm (Figure S6b), obviously higher than that of Ag NPs in Ag/ZIF-8. This comparison indicates that the capping agent MPA causes the uniform and nanoscale dispersion of Ag particles, [**4**] and meanwhile ZIF-8, rather than carbon black, can assist in further reducing the size of Ag NPs. For comparison, the Ag/C (with similar size of Ag NPs) was synthesized using a modified protocol according to reference, Figure S9a clearly shows that Ag nanoparticles are uniformly distributed on the Ag/C with an average size of 4.4 nm (Figure S9b), which is close to the Ag NPs in Ag/ZIF-8.

Figure S7 presents the linear sweep voltammetry (LSV) curves of Ag/ZIF-8 modified electrode in Ar- and $CO_2$-saturated KCl (0.5 M) electrolyte. The current density started to increase from approximately −0.7 V versus the reversible hydrogen electrode (RHE) in the Ar-saturated electrolyte, which is contributed by the hydrogen evolution reaction (HER). By contrast, the electrode in the $CO_2$-saturated electrolyte shows significantly higher current density owning to the occurrence of additional $CO_2$RR, which implies that Ag/ZIF-8 is an excellent $CO_2$RR catalyst.

The $CO_2$RR performance of the catalysts was evaluated at different potentials in a two-compartment cell with 0.5 M KCl at room temperature. In the experiment, CO is the major product and $H_2$ is the byproduct derived from the competitive HER. There are no liquid products detected by $^1$H NMR spectroscopy. To better compare the $CO_2$RR performance of Ag/ZIF-8, we evaluated another two catalysts, *i.e.*, ZIF-8, and Ag/C, toward the $CO_2$RR. As shown in **Fig. 5a**, the current densities of Ag/ZIF-8 are slightly higher than those of Ag/C, but both of them are obviously higher than those of ZIF-8. This proves that Ag is the major contributor to the current density derived from $CO_2$RR and HER.

As shown in **Fig. 5b**, the Ag/C shows a maximum CO Faradaic efficiency (CO FE) of 87.6% at −0.88 V (vs. RHE), while the maximum CO FE for Ag/ZIF-8, with a similar Ag loading to Ag/C (Table S1), achieves to 92.3% at the same potential. Actually, Ag/ZIF-8 has higher CO FEs than Ag/C at all the applied potentials. Without the Ag NPs, ZIF-8 shows a maximum CO FEs of only 65% at −1.2V, which is line with the previous report[14] but largely inferior to Ag/ZIF-8 and Ag/C. Furthermore, CO partial current density ($j_{CO}$) was calculated by multiplying the CO FE by the total current density and plotted against the test potentials as shown in **Fig. 5c**. The partial current density for CO ($j_{CO}$) production increases with the increase of negative working potential (**Fig. 5c**). Among the three catalysts, Ag/ZIF-8 has the highest $j_{CO}$ in the applied potential range and reaches a maximum CO FE of −18.5 mA/cm$^2$ at −1.36V. For comparison, we have also listed the previous performance of similar catalysts for $CO_2$RR in supporting information Table S2.

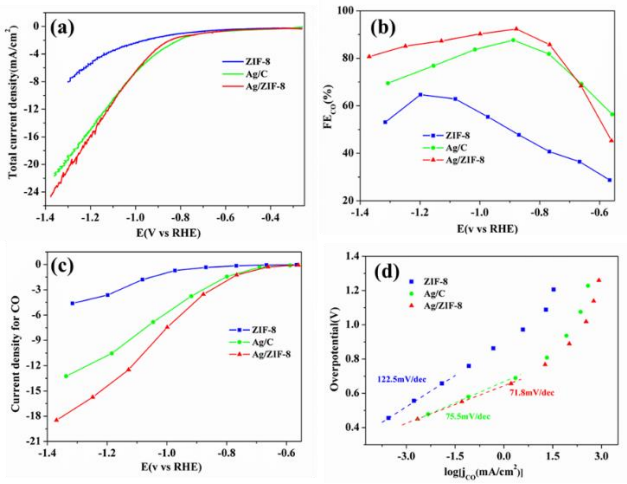


**Fig. 5.** (a) LSV curves of ZIF-8, Ag/C and Ag/ZIF-8 in $CO_2$- saturated 0.5 M KCl, scanning rate:10mV/s, (b)$FE_{CO}$ at various potentials, (c) Current density for CO production on ZIF-8, Ag/C and Ag/ZIF-8, (d) Tafel plots of CO production for ZIF-8, Ag/C and Ag/ZIF-8.

Kim *et. al.*, synthesize Ag NPs/C with the help of cysteamine as the thiol-containing anchoring agent, but the cysteamine/$Ag^+$ is very low, resulting in negligible $Ag_2S$-like phase. For Ag/ZIF-8, the amount of $Ag_2S$-like phase is relatively high, but their stability may be susceptible to the $CO_2$RR condition. To verify the speculation, XPS was employed to characterize the used Ag/ZIF-8 catalyst after $CO_2$RR under the maximum applied potential, i.e., −1.36 V (Figure S8). The S2p XPS spectrum (Figure S8b) is more informative than Ag 3d spectrum (Figure S8a). The almost-complete disappearance of $S2p_{3/2}$ peak at 161 eV indicates that the $Ag_2S$-like was reduced into Ag by the negative potential (−1.36 V, Figure S8b). However, the MPA still adsorbed on the Ag NPs, as shown by the peak at 163 eV (Figure S8b). It comes as no surprise that the XPS spectra exhibits the presence of sulfate species (above 167 eV, Figure S8b), because they are mainly contributed by the sulfonic acid ($SO_3H$) groups in Nafion mixed with the catalyst. For potentials less negative than −1.36 V, the $Ag_2S$-like phase can't be always reduced into Ag. Therefore, we concluded that the species that participate $CO_2$RR may be $Ag_2S$-like phase or Ag, which depends on the $CO_2$RR potential. The effect of sulfation [**22-23**] or Ag-S interaction [**4**], either positive or negative, on the $CO_2$RR performance can't be excluded, but it will not cover the catalytic advantage of Ag/ZIF-8 over Ag/C because Ag NPs in both catalysts were prepared by using MPA and would not exhibit too many differences. The small-sized Ag NPs (3.9 nm) on ZIF-8 and the possible synergistic effect between Ag NPs and ZIF-8 can account for the catalytic advantage of Ag/ZIF-8 over Ag/C.

When the Ag(0) can exposed to ZIF-8, the synergistic effect between Ag NPs and the ZIF-8 can be a possible positive factor for enhanced $CO_2$RR performance [**24**].

To obtain insights into the electrokinetic mechanism for $CO_2$ reduction on these catalysts, Tafel plots (A Tafel plot relates to overpotential versus logarithm of the partial current density of a specific product) for them were displayed in **Fig. 5d**. The plot of the ZIF-8 is linear over the range of overpotentials from 0.45 to 0.65V with a slope of 122.5 mV/dec, indicating that the initial electron transfer of $CO_2$ activation is the rate-determining step. Tafel slopes of Ag/C and Ag/ZIF-8 are 75.5 and 71.8 mV/dec, respectively. This dramatic decrease in Tafel slopes proves that the introduction of thiol-capped Ag NPs largely accelerates the initial electron transfer to a $CO_2$ molecule. These silver-containing catalysts exhibit similar Tafel slopes, which suggest that Ag is the major contributor to the $CO_2$RR.

The long-term stabilities of the Ag/ZIF-8 were evaluated at −0.88V vs. RHE for 10 h (**Fig. 6**). Within 10 h of reaction, the current density declines slightly from 3.5 mA to 3.1 mA. Meanwhile, the Ag/ZIF-8 exhibits slightly loss of $FE_{CO}$ from 92.3% to 82.2%. The above results indicate that the Ag/ZIF-8 possesses a relatively good stability.

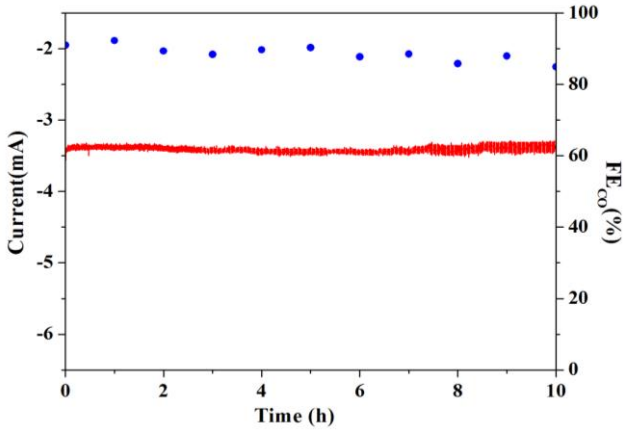


**Fig. 6.** Stability test of Ag/ZIF-8 at −0.88 V (vs. RHE).

## Conclusion

In summary, ultrafine thiol-capped Ag nanoparticles uniformly decorated ZIF-8 (Ag/ZIF-8) was successfully prepared and applied to $CO_2$RR for the first time. The major product CO on the Ag/ZIF-8 catalyst could achieve a high Faradaic efficiency of 92.3% at a moderated potential of −0.88 V with a current density of 3.8 mA/cm$^2$. The Ag/ZIF-8 catalyst showed higher CO faradaic efficiency and current density than ZIF-8 and Ag/C. What's more, the Ag/ZIF-8 catalyst's stability is good as it can serve a working lifetime without large deactivation for 10 hours. Overall, the strategy developed here demonstrated a novel and convenient route to synthesize supported small-sized Ag NPs to enhance $CO_2$RR performance of Ag.

**Acknowledgements**

The authors are grateful for the financial support by the National Natural Science Foundation of China (Grant No. 51901206) and the fund by the Taihu Electric Corporation 0001.

**Conflicts of interest**

There are no conflicts to declare.

**Supporting information**

Supporting information are available online at journal website.

**Keywords**

$CO_2$ reduction, electrocatalysis, ZIF-8, Ag nanoparticles, Ag/ZIF-8, CO.

**Received: 25 March 2020**
**Revised: 03 May 2020**
**Accepted: 04 May 2020**

**References**

1. Lim, R. J.; Xie, M.; Sk, M. A.; Lee, J.-M.; Fisher, A.; Wang, X.; Lim, K. H., *Catal. Today,* **2014**, *233*, 169.
2. Goeppert, A.; Czaun, M.; May, R. B.; Prakash, G. K.; Olah, G. A.; Narayanan, S. R.; *J. Am. Chem. Soc.,* **2011**, *133*, 20164.
3. Qiao, J.; Liu, Y.; Hong, F.; Zhang, J.; *Chem. Soc. Rev.* **2014**, *43* , 631.
4. Kim, C.; Jeon, H. S.; Eom, T.; Jee, M. S.; Kim, H.; Friend, C. M.; Min, B. K.; Hwang, Y. J.; *Journal of the American Chemical Society,* **2015**, *137*, 13844.
5. Gao, D.; Zhou, H.; Cai, F.; Wang, J.; Wang, G.; Bao, X.; *ACS Catal.,* **2018**, *8*, 1510.
6. Zhu, W.; Michalsky, R.; Lv, H.; Guo, S.; Wright, C. J.; Sun, X.; Peterson, A. A.; Sun, S.; *J. Am. Chem. Soc.,* **2013**, *135*, 16833.
7. Quan, F.; Zhong, D.; Song, H.; Jia, F.; Zhang, L.; *Journal of Materials Chemistry A,* **2015**, *3,* 16409.
8. Zhang, Y.; Hu, L.; Han, W.; *J. Mater. Chem. A,* **2018,** *6* (46), 23610.
9. Liu, S.; Tao, H.; Zeng, L.; Liu, Q.; Xu, Z.; Liu, Q.; Luo, J. L.; *J. Am. Chem. Soc.,* **2017**, *139*, 2160.
10. Kim, C.; Jeon, H. S.; Eom, T.; Jee, M. S.; Kim, H.; Friend, C. M.; Min, B. K.; Hwang, Y. J.; *J. Am. Chem. Soc.,* **2015**, *137,* 13844.
11. Hatsukade, T.; Kuhl, K. P.; Cave, E. R.; Abram, D. N.; Feaster, J. T.; Jongerius, A. L.; Hahn, C.; Jaramillo, T. F.; *Energy Technology,* **2017**, *5,* 955.
12. Lu, Q.; Rosen, J.; Zhou, Y.; Hutchings, G. S.; Kimmel, Y. C.; Chen, J. G.; Jiao, F.; *Nat. Commun.,* **2014**, *5,* 3242.
13. Luan, C.; Shao, Y.; Lu, Q.; Gao, S.; Huang, K.; Wu, H.; Yao, K.; *ACS Appl Mater Interfaces,* **2018**, *10,* 17950.
14. Wang, Y.; Hou, P.; Wang, Z.; Kang, P.; *Chemphyschem,* **2017**, *18,* 3142.
15. Kornienko, N.; Zhao, Y.; Kley, C. S.; Zhu, C.; Kim, D.; Lin, S.; Chang, C. J.; Yaghi, O. M.; Yang, P.; *J. Am. Chem. Soc.,* **2015**, *137,* 14129.
16. Jiang, X.; Li, H.; Xiao, J.; Gao, D.; Si, R.; Yang, F.; Li, Y.; Wang, G.; Bao, X.; *Nano Energy,* **2018**, *52,* 345.
17. Wang, Z.; Huang, J.; Guo, Z.; Dong, X.; Liu, Y.; Wang, Y.; Xia, Y.; *Joule,* **2019**, *3,* 1289.
18. Lanas, S. G.; Valiente, M.; Tolazzi, M.; Melchior, A.; *J. Therm. Anal. Calorim.,* **2018**, *136,* 1153.
19. Battocchio, C.; Meneghini, C.; Fratoddi, I.; Venditti, I.; Russo, M. V.; Aquilanti, G.; Maurizio, C.; Bondino, F.; Matassa, R.; Rossi, M.; Mobilio, S.; Polzonetti, G.; *The Journal of Physical Chemistry C,* **2012**, *116,* 19571.
20. Gao, J.; Zhao, S.; Guo, S.; Wang, H.; Sun, Y.; Yao, B.; Liu, Y.; Huang, H.; Kang, Z.; *Inorganic Chemistry Frontiers,* **2019**, *6,* 1453.
21. Battocchio, C.; Fratoddi, I.; Fontana, L.; Bodo, E.; Porcaro, F.; Meneghini, C.; Pis, I.; Nappini, S.; Mobilio, S.; Russo, M. V.; Polzonetti, G.; *Phys. Chem. Chem. Phys.,* **2014**, *16,* 11719.
22. Hu, L.; Zhang, Y.; Han, W.; *New J. Chem.,* **2019**, *43,* 3269.
23. Zeng, L.; Shi, J.; Luo, J.; Chen, H.; *Journal of Power Sources,* **2018**, *398*, 83.
24. Jiang, X.; Wu, H.; Chang, S.; Si, R.; Miao, S.; Huang, W.; Li, Y.; Wang, G.; Bao, X.; *J. Mater. Chem. A,* **2017**, *5*, 19371.